

MICROBOTICS

Powerful, soft combustion actuators for insect-scale robots

Cameron A. Aubin¹, Ronald H. Heisser¹, Ofek Peretz^{1,2}, Julia Timko¹, Jacqueline Lo¹, E. Farrell Helbling³, Sadaf Sobhani¹, Amir D. Gat², Robert F. Shepherd^{1*}

Insects perform feats of strength and endurance that belie their small stature. Insect-scale robots—although subject to the same scaling laws—demonstrate reduced performance because existing microactuator technologies are driven by low-energy density power sources and produce small forces and/or displacements. The use of high-energy density chemical fuels to power small, soft actuators represents a possible solution. We demonstrate a 325-milligram soft combustion microactuator that can achieve displacements of 140%, operate at frequencies >100 hertz, and generate forces >9.5 newtons. With these actuators, we powered an insect-scale quadrupedal robot, which demonstrated a variety of gait patterns, directional control, and a payload capacity 22 times its body weight. These features enabled locomotion through uneven terrain and over obstacles.

Swarms of centimeter-scale robots that can crawl (1–3), jump (4–7), and fly (8, 9) like insects have the potential to survey and report on phenomena of interest and even influence their local environment. Applications span an array of fields, including healthcare, exploration, communication, and agriculture (10). For example, broad area surveillance of local soil conditions could ensure exact application of nitrogen, reducing the impact of excessive fertilizer use. Other robots could be deployed in hazardous or inaccessible environments to scan for signs of life in a search-and-rescue mission. To achieve the transportation distances (hundreds of meters) and speeds (tens of centimeters per second) required to realize their potential at costs that are affordable for large quantities (hundreds) of robots, substantial improvements to the size, weight, power, and fabrication limitations of microactuators are needed.

Because of the payload constraints, scaling laws, and manufacturing restrictions relevant to insect-scale robots, the state of the art in microactuator technologies is dominated by bespoke devices (11–13). Popular electromechanical options for actuation at this scale include piezoelectric bimorphs and dielectric elastomer actuators (DEAs). These microactuators operate at high frequencies ($f = 10$ to 1000 Hz) and demonstrate respectable power densities ($\Pi_{\text{max}} \sim 600 \text{ W kg}^{-1}$) (2, 14). However, DEAs and piezoelectric bimorphs lag behind their biological counterparts in some key areas. Individual actuations are low-force ($F \ll 1\text{N}$) and low-amplitude ($\delta_{\text{piezo}} \ll 10\%$, $\delta_{\text{DEA}} < 25\%$), and they must be operated near resonance ($f \sim 100$ to 1000 Hz) to achieve suitable per-

formance (2, 9, 15–17). These limitations result in a lower average work (energy) density. Still, other microactuators used in robotics—including electrostatic (e.g., comb drives and parallel plates), thermal (e.g., phase change, shape-memory alloys and polymers), and magnetic actuators (e.g., magnetostrictive, external field)—lack either the cycling speeds, force, and/or displacement to perform meaningful work (15, 18, 19).

Chemical fuels represent a possible solution to these problems. The energy density of combustibles such as methanol ($\Gamma = 22.7 \text{ MJ kg}^{-1}$) or butane ($\Gamma = 49.5 \text{ MJ kg}^{-1}$) greatly exceeds that of electrical sources [e.g., Li-ion microbatteries, $\Gamma < 1.0 \text{ MJ kg}^{-1}$ (20)]. Centimeter-scale internal combustion engines (ICEs) have previously been explored for use in micro-aerial vehicles, portable devices, and small spacecraft. They suffer, however, from several issues, including leakage versus stiction, thermal management, efficiency, material restrictions, weight, and fabrication complexity, that make them incompatible with insect-scale robots (21). Soft robots, often actuated through volumetric expansion, have also been successfully driven by using combustible chemical fuels (22–24), as have soft pumps (25, 26) and even soft haptic displays (27).

Despite clear utility, the combustion of chemical fuels has seldom been explored in robots at or below the centimeter scale. Some recent examples use only a single, noncyclic combustion event for a one-time actuation (28, 29). Other robots such as the Octobot (30) and RoBeetle (3) are untethered, housing onboard fuel reserves, but contain low-frequency and low-force actuators. The large energetic potential of chemical fuels has yet to be fully exploited within this domain.

We present a lightweight ($m = 325 \text{ mg}$), power-dense ($\Pi_{\text{stroke}} = 277.2 \text{ kW kg}^{-1}$), high-frequency microactuator (Fig. 1) driven by the combustion of chemical fuels and describe its

integration into an insect-scale robot. The actuator can produce forces greater than 9 N—an order of magnitude larger than existing microactuators of similar size, weight, and/or material composition—in submillisecond impulses. It operates at a range of desirable frequencies and can exceed 100 Hz.

Actuator fabrication and operation

We used a CLIP (continuous liquid interface production) 3D printer and a V-0 flame-resistant resin (EPX-86 FR; Carbon, Inc.) to fabricate the microactuators (Fig. 1A). This combination of material and manufacturing strategy gave us the ability to rapidly and cost-effectively produce small, lightweight, high-resolution combustion chamber bodies with favorable thermal properties. We determined the precise geometry of the roughly cylindrical combustion chambers (volume $V = 0.09 \text{ mL}$) with early qualitative tests [supplementary materials (SM) section S7] (27) through which we evaluated flame propagation and venting behavior, as well as actuator integrity. We fitted these chambers with sparking electrodes, a flame arrestor module, and a thin elastomer (Dragon Skin 10, Smooth-On) membrane that served as the actuating surface. The complete manufacturing process for these devices can be found in SM section M1.

Much like a conventional ICE, the operation of the microactuator starts with the transfer of fuel—a mixture of gaseous methane and oxygen—into the combustion chamber (Fig. 1B). This process is facilitated by off-board mass flow controllers (MFCs) that continuously deliver prescribed amounts of fuel into the actuators through a thin length of tubing (fig. S1). This fuel is ignited with a small spark generated by offboard high-voltage ($U_{\text{spark}} \sim 800$ to 1200 V, depending on manufacturing variations) electronics connected to the electrode wires (fig. S2). The ensuing exothermic reaction causes product gases to expand and the elastomer membrane to inflate simultaneously (Fig. 1C and movie S1). This rapid (inflation time, $t_{\text{inflate}} \leq 0.55 \text{ ms}$), piston-like actuation of the membrane can be used to powerfully drive end effectors, launch objects, or otherwise perform work. The actuation process ends when the product gases passively vent (deflation time, $t_{\text{deflate}} \sim t_{\text{inflate}}$) from the combustion chamber, and the cycle is then repeated. Passive flame quenching—defined here as the dissipation of flame fronts without the use of valves or active mechanisms—allows this process to occur continuously and repeatedly at high frequencies. We achieved passive quenching in our system through a combination of factors: (i) limiting flame propagation with a sub-milliliter combustion chamber volume, (ii) constructing the actuator from a material with flame-quenching properties, (iii) application of a dedicated onboard flame arrestor,

¹Sibley School of Mechanical and Aerospace Engineering, Cornell University, Ithaca, NY 14853, USA. ²Faculty of Mechanical Engineering, Technion-Israel Institute of Technology, Haifa 3200003, Israel. ³Department of Electrical and Computer Engineering, Cornell University, Ithaca, NY 14853, USA.

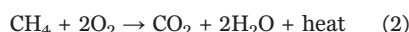
*Corresponding author. Email: rfs247@cornell.edu

and (iv) usage of fuel-lean reactant chemistries. We further discuss the design decisions that contributed to passive quenching in SM section S1.

Actuator characterization

The performance of the actuator can be dynamically modulated by driving it at different frequencies or at different fuel-oxidizer concentrations, denoted by ϕ :

$$\phi = \frac{\left(\frac{n_{\text{fuel}}}{n_{\text{oxid}}}\right)_{\text{actual}}}{\left(\frac{n_{\text{fuel}}}{n_{\text{oxid}}}\right)_{\text{stoich}}} \quad (1)$$



where ϕ is the historically defined fuel-air equivalence ratio (37), and n_{fuel} and n_{oxid} represent moles of methane and oxygen, respectively. When $\phi = 1$, the system will react stoichiometrically (Eq. 2). Ratios corresponding to $\phi < 1$ are termed “fuel lean” because the reaction concludes with a surplus of oxygen. We operate our actuator at fuel-lean equivalence ratios, typically between $0.2 < \phi < 0.6$, because this limits the production of unwanted by-products (e.g., soot, NO_x compounds); reduces the risk of flashback, in which flames reverse propagate up feed lines toward the fuel source; and decreases the probability of damaging the actuator. Figure 1D shows how increasing the equivalence ratio toward stoichiometric levels while maintaining actuation frequency and gas flow rate corresponds with an increase in membrane deformation. A greater fuel volume leads to an increase in the heat of combustion, which results in a greater expansion of product gases and an increase in membrane inflation.

We characterized the performance of the actuator by conducting membrane displacement (Fig. 1E) and blocked-force testing (Fig. 1F) across a range of equivalence ratios and frequencies (figs. S3 to S5). We captured displacement data using a high-speed camera and processed the video in ImageJ. The actuation frequency was dynamically adjusted with an Arduino microcontroller interfacing with the high-voltage-generating electronics. Custom LabVIEW code allowed for control of the fuel's equivalence ratio and flow rate by way of the MFCs. The reported reduction in membrane displacement with increasing frequency was a consequence of the experiments being conducted at a constant fuel flow rate ($Q = 2 \pm 0.1 \text{ ml s}^{-1}$, composition dictated by ϕ); for a set volumetric flow rate, a higher rate of combustion corresponds to a smaller volume of fuel being consumed in each combustion event. Adjusting the flow rate allowed us to achieve any combination of frequencies and displacements within the ranges of $0 < f < 100 \text{ Hz}$ and $\sim 0.75 <$

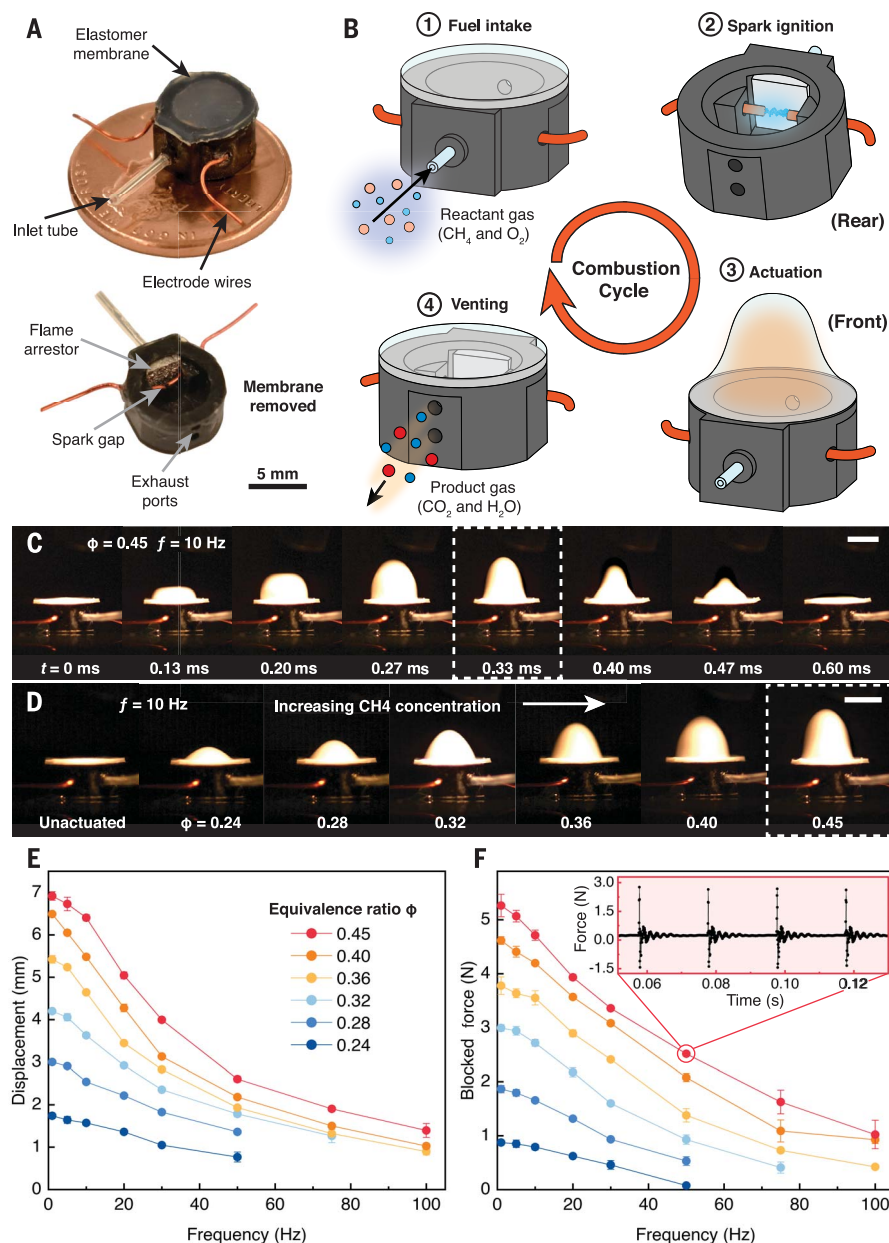


Fig. 1. Operation and characterization of the combustion-driven microactuator. (A) Front (top) and rear (bottom) view of the actuator and its component materials. (B) Diagram of the combustion actuation process. (C) Time-lapse image of a single actuation cycle. t , time. (D) Images of the actuator at different maximum displacements for a range of fuel-oxidizer (equivalence) ratios (ϕ). Photos were taken at the same actuation frequency $f = 10 \text{ Hz}$. The dotted boxes indicate matching images in (C) and (D), which both occurred at $\phi = 0.45$ and $f = 10 \text{ Hz}$. Scale bars [(C) and (D)], 5 mm. (E) Actuator displacement and (F) blocked force as a function of different frequencies for a series of equivalence ratios ($n = 5$ actuator tests, error bars = 1 SD). The inset plot shows the force profile achieved when tested at $\phi = 0.45$ and $f = 50 \text{ Hz}$. Data are not available above $f = 50 \text{ Hz}$ for $\phi = 0.24$ and 0.28 or above $f = 75 \text{ Hz}$ for $\phi = 0.32$ because the volume of fuel in the actuator under these conditions is too small to sustain combustion.

$\delta < 7 \text{ mm}$. These ranges are not fundamental limitations to our technique but represent practical limitations of our initial experimental setup. The peak membrane displacement that we report, $\delta = 7 \text{ mm}$, corresponds to a linear strain of the hyperelastic membrane of $y = 180\%$ and a total actuator elongation of

$z = 140\%$, which is greater than contemporary microactuators employing soft materials (16) but far less than the ultimate strain ($y_{\text{ult}} \sim 1000\%$) of the silicone copolymer we used in our membrane.

We measured the blocked force of these actuators using a high-precision load cell (fig. S4;

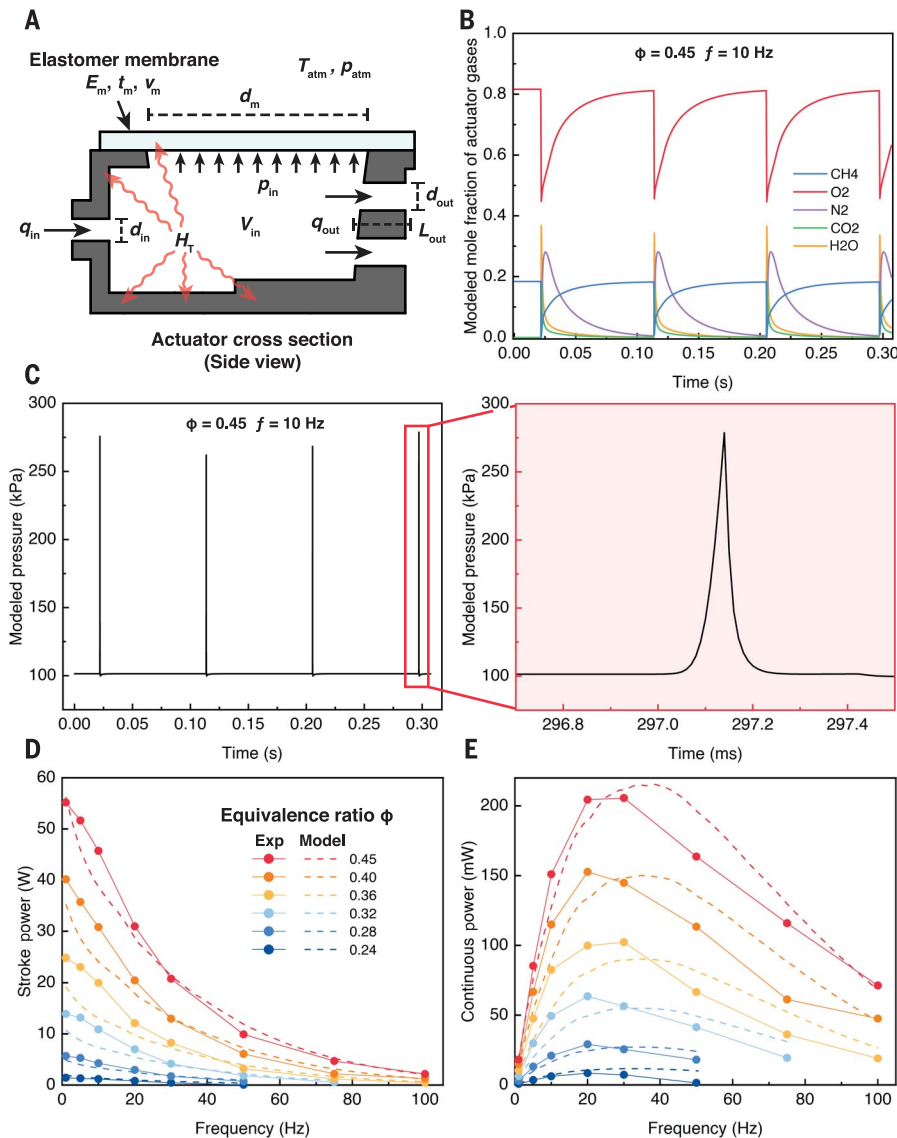


Fig. 2. Model of microactuator performance. (A) A schematic diagram of the model actuator used in our analysis. E_m , Young's modulus of the elastomer membrane; t_m , membrane thickness; v_m , Poisson's ratio of membrane material; d_m , membrane diameter; T_{atm} , atmospheric temperature; p_{atm} , atmospheric pressure; q_{in} , gas flow rate into actuator; q_{out} , flux out of actuator; p_{in} , internal actuator pressure; V_{in} , internal volume of actuator; d_{in} and d_{out} , diameters of the inlet and outlet ports, respectively; L , the length of the exhaust port; H_T , heat-transfer coefficient. (B) The change in the concentration of reactant and product gases during actuation at $f = 10$ Hz as predicted by our model. (C) The internal pressure of our actuator during operation, modeled as a function of time. A magnified inset is provided for clarity. (D) The experimentally derived stroke-power and (E) continuous-power output of our actuator compared with our model predictions. A magnified image of the lowest equivalence ratios in (D) is shown in fig. S12.

SM section M4) at constant Q for different f and ϕ values. Exemplary force profiles can be seen as an inset in Fig. 1F and fig. S5. The peak force that we detected during blocked-force testing, $F_{max} = 9.5$ N at $\phi = 0.6$ (fig. S5), is an order of magnitude greater than that of previously reported high-frequency micro-actuators (SM section S2). Some of our testing at $\phi = 0.6$ resulted in tearing and delamination of the membrane; we consequently denote the actuator's performance at this equivalence

ratio as being an upper bound limited by our present system's durability. As shown in Fig. 1F, the actuator can continually produce forces in excess of $F = 5$ N at a lower equivalence ratio of $\phi = 0.45$ without accruing membrane damage. Durability tests and subsequent SEM analysis of the membranes confirmed that the actuator can continuously operate for more than 750,000 cycles ($\phi = 0.30$ and $f = 25$ Hz) without any perceived drop in performance (figs. S6 and S7 and SM section M5).

We calculated the microactuator's work and power output (figs. S8 and S9 and SM section S4) using the equations:

$$W = \frac{1}{2} F_b \delta \quad (3)$$

$$P_{stroke} = \frac{1}{2(t_{inflation})} F_b \delta \quad (4)$$

$$P_{cont} = \frac{1}{2} F_b \delta f \quad (5)$$

where δ , F_b , $t_{inflation}$, and f are the actuator's displacement, blocked force, inflation time, and operating frequency, respectively. We calculated a maximum work output of ~ 30 mJ when the actuator is driven at $\phi = 0.6$ (18.2 mJ at $\phi = 0.45$), which corresponds to a peak energy density of 91.4 J kg $^{-1}$. We further characterized actuator power using two metrics: stroke power, P_{stroke} , calculated only over the time frame during which actuation is occurring; and continuous power, P_{cont} , calculated over the entire operational period. Because of our rapid, submillisecond actuation times, the traditional P_{cont} metric inadvertently includes large amounts of idle time in its calculation (e.g., an actuator operating at $f = 10$ Hz would spend less than 1% of its operating time actuating). Conversely, the P_{stroke} metric narrows our focus to relevant, but brief, windows of time in the actuation cycle. Used together, both metrics give a more complete picture of actuator performance.

From our experiments, we measured a maximum power of $P_{cont} = 288.7$ mW ($\phi = 0.6$, $f = 20$ Hz) and $P_{stroke} = 90.1$ W ($\phi = 0.6$; fig. S9). The corresponding power densities are $\Pi_{cont} = 888.3$ W kg $^{-1}$ and $\Pi_{stroke} = 277.2$ kW kg $^{-1}$, respectively. The peak theoretical continuous power is $P_{cont-max} = 2.97$ W ($\Pi_{cont-max} = 9.1$ kW kg $^{-1}$) (SM section S4). We also estimated the maximum efficiency of our actuator at $\sim 4\%$ (figs. S8 and S9 and SM section S4); the magnitude of this value is a normal consequence of combustion in submilliliter volumes (32), but is also affected by our open-venting configuration, the lack of compression in our system, and our fuel-lean equivalence ratios.

Modeling the actuator

To gain insight into the dominant physical phenomena that govern combustion actuation, we derived a simplified system model that takes into account the elasticity of the membrane, the fuel flow within the cell, the energy released by ignition of the fuel, and the effects of the internal pressure and temperature within the microactuator. Using this model, we were able to predict values for the displacement of the actuator membrane, the blocked force of the actuator, the jumping height of the robot, and the exhaust flow rate as functions of the actuation

frequency and fuel equivalence ratio. The model consists of three coupled segments: (i) chamber elasticity and deformation in response to an increase in internal pressure, (ii) fluidic flow balance, and (iii) energy balance of the heat of combustion and its conversion into thermal energy and pressure. The governing equations for these segments are derived and summarized in SM section S5. Relevant code for our models can be found in our online repository (33).

Figure 2A shows a schematic diagram of our model microactuator, complete with relevant variables. Using our model, we were able to predict the concentrations of major reactant and product species (Fig. 2B; $\phi = 0.45$, $f = 10$ Hz) (a magnified image of this data during the combustion window can be seen in fig. S10), as well as the rapidly increasing internal pressure of the actuator (Fig. 2C) when undergoing combustion. The duration of these pressure spikes ($t_{\text{model}} \sim 0.15$ ms versus $t_{\text{reaction}} \sim 0.12$ ms and $t_{\text{inflation}} \sim 0.33$ ms) shows that our modeled data agree with our observed reaction kinetics. Using this pressure data, we were able to predict the blocked force of our actuators and compare it with our experimentally acquired force data (fig. S11). Our model also takes into account the elastic properties of the rapidly deforming membrane and can predict the free displacement of the membrane during combustion (fig. S11). Performing calculations with this modeled data, as described above for our experimental data, allowed us to generate predictions for the work and power output of our modeled actuator (Fig. 2, D and E, and fig. S12). The trends and magnitude of our modeled data accurately approximate our experimental results.

We also characterized the thermal activity of our actuator using a combination of experimental measurements and modeled data to calculate the external and internal wall temperatures, as well as the gas temperatures during combustion (fig. S13, SM section S6). The chamber temperature is an important consideration for device durability; at frequencies exceeding 50 Hz (for all equivalence ratios), the steady-state temperature of the actuator rises to a level that can result in ignition and burning of the chamber. We therefore recommend intermittent operation at these frequencies, allowing several seconds of cooling for every 1 to 2 min of actuation. Notably, the actuators can be operated with impunity at frequencies below 50 Hz (as evidenced by our 8.5-hour, 750,000-cycle durability test), and the frequency limitations of the robot do not put it in danger of thermal damage.

Powering an insect-scale robot

To demonstrate the effectiveness of our microactuators in powering insect-scale devices, we designed and fabricated a combustion-driven quadrupedal robot (Fig. 3A). The assembly

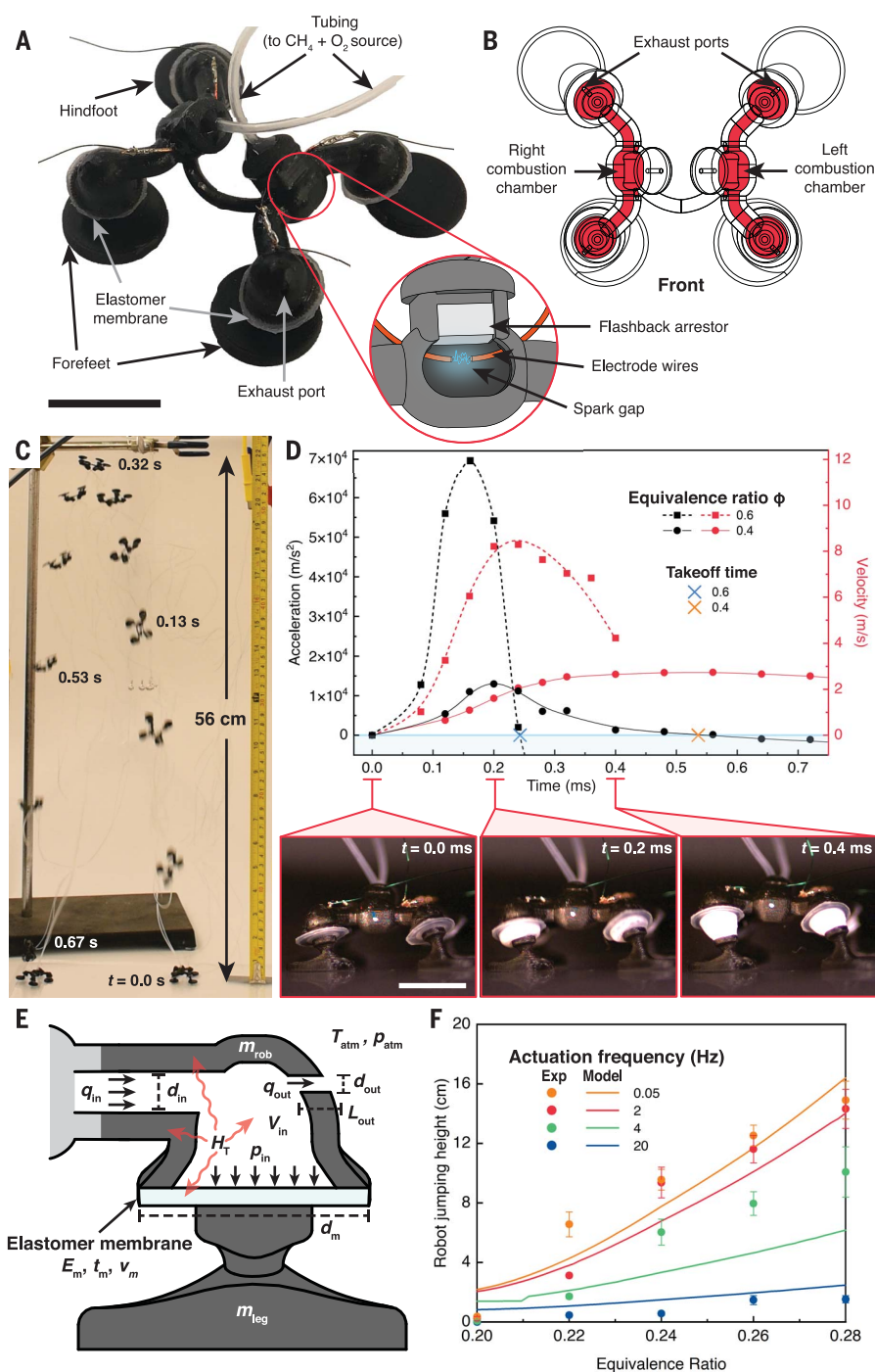


Fig. 3. Jumping performance of the quadrupedal, insect-scale robot. (A) Photograph of the robot with component parts labeled. A schematic of the interior of the combustion chamber is also provided. Scale bar, 1 cm. (B) A transparent diagram of the robot, with the two independent combustion chambers highlighted in red. (C) Time-lapse image of our robot performing a 56-cm vertical leap. (D) Acceleration (black) and velocity (red) data of the robot body during takeoff at $\phi = 0.6$ (square data points) and 0.4 (circular data points). The associated images outlined in red depict a takeoff experiment at $\phi = 0.60$. Scale bar, 1 cm. (E) A schematic diagram of our idealized model robot leg. The variable definitions are the same as those in Fig. 2A, with the addition of m_{rob} , mass of the robot body, and m_{leg} , mass of the robot leg. (F) Modeled robot jumping height as a function of equivalence ratio for a series of actuation frequencies. Experimental data are depicted as solid circles ($n = 5$ robot tests; error bars, 1 SD), whereas a solid line denotes the height predicted by our model.

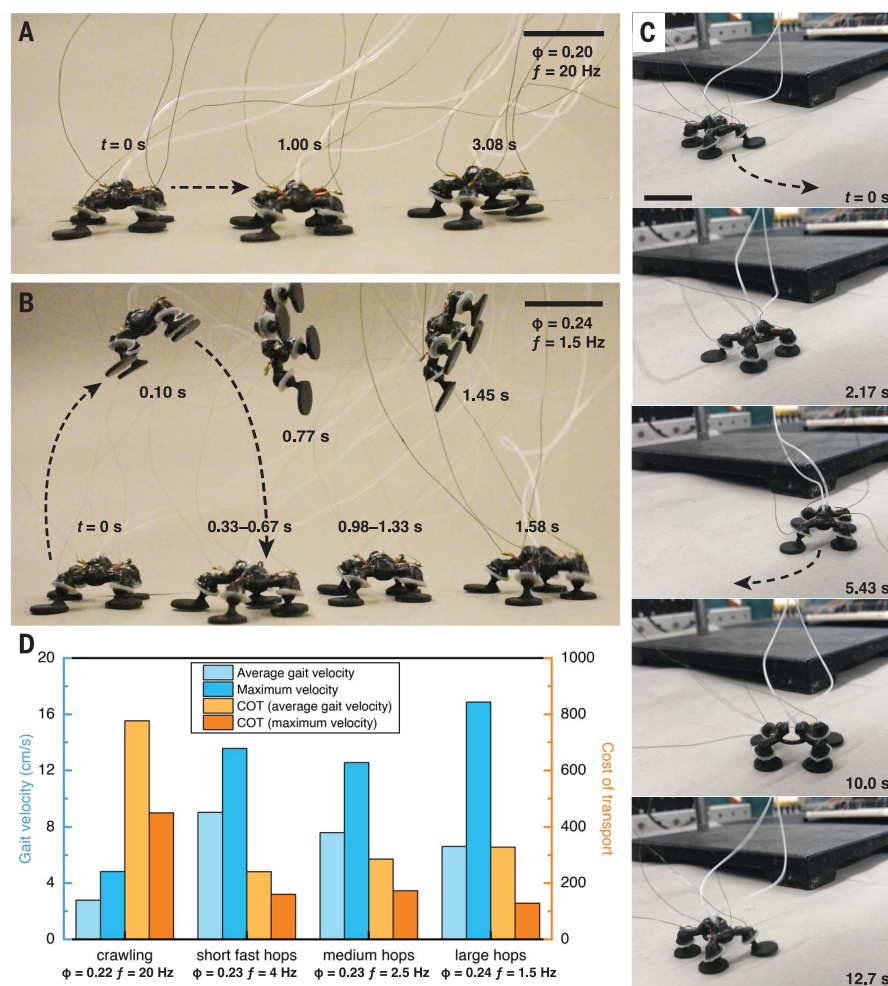


Fig. 4. Characterization of the robot's multigait functionality. (A) Timelapse image of the robot performing a crawling gait and (B) a hopping gait. In (B), the tethers have been dimmed in all but the rightmost image so as not to obscure the robot's trajectory. (C) Timelapse image of the robot performing a counterclockwise rotation, followed by a clockwise rotation. Scale bars [(A), (B), and (C)], 2 cm. (D) A graphical representation of the velocities and cost of transport of different gait patterns performed by the robot.

process and bill of materials was similar to that of the individual microactuators and is outlined in SM section M6 and fig. S14. The robot ($L = 29$ mm, $m = 1.6$ g) is composed of two symmetric halves connected by a curved, rigid linkage. The hollow interiors of these halves are distinct, functioning as separate combustion chambers that drive one front and one rear foot each (Fig. 3B). A methane and oxygen mixture is delivered through thin tubing into the two ellipsoidal drums at the center of the robot (the same two-MFC testing configuration is used to operate both the robot and the actuators; fig S1). Ignition is achieved by using the same sparking configuration as in the microactuator tests and results in the expansion of the elastomer membranes at either end of the chamber (Fig. 3, C and D). The robot geometry draws on several of the microactuators' design features, displaying similar internal volumes, vent hole configurations, actuation and combustion chamber

dimensions, and membrane dimensions (SM section S7). The four actuating feet of the robot are functionally similar to the micro actuators, but they are paired together and fed from a central chamber.

Varying the different input parameters (spark frequency f , equivalence ratio ϕ , fuel flow rate Q , and combustion chamber selection) creates different locomotion modes. For example, actuating both chambers simultaneously at large equivalence ratios ($\phi > 0.35$) resulted in a large vertical leap (Fig. 3C and movie S2), which allowed the robot to clear obstacles or land on top of elevated terrain (movie S3). While performing jumping experiments, the robot was able to achieve a maximum vertical height of 59 cm ($n = 4$, $SD = 0.96$ cm) and a horizontal distance of 16 cm, which are 20 and 5.5 times the robot's body length (BL), respectively (SM section M8). We used a high-speed camera to study the dynamics of the robot at the moment

of takeoff (movie S4). Figure 3D shows the acceleration and velocity of the robot's body when driven at two different equivalence ratios. The takeoff time—when the feet begin to leave the ground—corresponds to the moment when the instantaneous acceleration transitions from a positive to a negative value.

We estimated the jumping height of our robot by modifying our blocked-force actuator model (changing the dimensions of relevant parameters) and applying it to our quadruped architecture. Figure 3E shows an idealized schematic diagram of our robot's leg and foot, which we used in modeling the jumping dynamics. Conservation of momentum and conservation of energy were used to derive the maximum jumping height of the robot from its internal pressure at different actuation frequencies and equivalence ratios (SM section S5). The results are shown in Fig. 3F. Deviation of the experimental data from the model can largely be explained by the model's tendency to underestimate blocked-force values at lower equivalence ratios ($\phi = 0.26$ to 0.28) (fig. S11B).

When operated at lower equivalence ratios ($\phi < 0.35$) and higher frequencies ($1 \text{ Hz} < f < 30 \text{ Hz}$), the robot is capable of performing several distinct movement patterns, including a crawling, vibration-like gait and forward hopping sequences of different heights (Fig. 4, A and B, and movie S5). The robot can dynamically switch between these movement styles by modifying the fuel equivalence ratio and/or the sparking frequency. We were able to pre-program these movement patterns by hard-coding the sparking sequence.

By inducing combustion in only one of the robot's two chambers at a time, we demonstrated limited directional control. Figure 4C shows counterclockwise and clockwise turns that were generated by repeatedly actuating just the right or left side of the robot, respectively. This behavior is a consequence of the foot orientation, with the front (fore) feet angled inward toward the body's centerline and the rear (hind) feet angled away, resulting in an approximately trapezoidal footprint. Actuating one side of the robot causes the corresponding hindfoot and both forefeet (which jump together owing to their proximity) to leave the ground. The opposite hindfoot remains mostly stationary and serves as the pivot point around which the robot rotates. We were able to demonstrate several rotation-based movements, including a snake-like forward walk, a rapid 360° rotation, and a reversal of direction when the robot encountered an impassable route (movie S6).

We characterized the performance of four representative gaits that manifest through the inputs shown in Fig. 4D. The highest equivalence ratio used in our gait analysis testing was $\phi = 0.24$; larger ϕ values were reserved for vertical leaping. When performing a hopping

gait at this ϕ , our robot demonstrated a maximum velocity of 16.9 cm s^{-1} , or 5.8 BL s^{-1} . For this gait, the cost of transport—a standard metric for the energy efficiency of moving bodies [defined as (input power)/(mass \times gravity \times velocity)]—was 128.8 (SM sections S8 and S9 and table S3). While executing a crawling gait, the robot demonstrated a maximum carrying capacity of 36 g, which is more than 22 times the robot's body weight (movie S7). Additionally, we tested our robot on a variety of surfaces, including acrylic, high-friction sandpaper, rubber, and sand (movie S8 and table S4).

We compared our robot's maximum horizontal velocity during crawling and hopping, along with its vertical leaping capabilities, with that of other robots in the literature (figs. S15 and S16). The robots that we used in these comparisons are summarized in tables S5 and S6. Notably, our robot can both crawl at high speeds and perform large vertical leaps. The crawling robots in our literature comparison lack the capacity to leap in any meaningful way. Similarly, most of the jumping robots shown in our comparison do not possess alternative locomotion capabilities. Our robot's multigait functionality is a direct result of the high-force and high-frequency capabilities of the embedded actuators.

Our actuators possess several advantages over existing systems that are used to power insect-scale devices: (i) the use of 3D printing as the dominant fabrication strategy allows for ease of scalability and integration with other systems; (ii) a soft actuation surface allows for device durability and a nondestructive means of interfacing with the environment; and (iii) the combination of high actuation speeds, forces, displacements, and frequencies leads to high power densities. When incorporated into a quadrupedal robot, the actuators enable multimodal locomotion and obstacle avoidance.

REFERENCES AND NOTES

1. B. Goldberg et al., *IEEE Robot. Autom. Lett.* **3**, 987–993 (2018).
2. X. Ji et al., *Sci. Robot.* **4**, eaa6451 (2019).
3. X. Yang, L. Chang, N. O. Pérez-Arancibia, *Sci. Robot.* **5**, eaba0015 (2020).
4. R. Kurniawan et al., "An Untethered 216-mg Insect-Sized Jumping Robot with Wireless Power Transmission" in 2020 *IEEE/RSJ International Conference on Intelligent Robots and Systems (IROS)*, Las Vegas, NV, 24 October 2020 to 24 January 2021, pp. 7881–7886; <https://doi.org/10.1109/IROS45743.2020.9341238>.
5. M. Noh, S.-W. Kim, S. An, J.-S. Koh, K.-J. Cho, *IEEE Trans. Robot.* **28**, 1007–1018 (2012).
6. J.-S. Koh et al., *Science* **349**, 517–521 (2015).
7. M. Kovac, M. Fuchs, A. Guignard, J.-C. Zufferey, D. Floreano, "A miniature 7g jumping robot," 2008 *IEEE International Conference on Robotics and Automation*, Pasadena, CA, 19 to 23 May 2008, pp. 373–378; <https://doi.org/10.1109/ROBOT.2008.4543236>.
8. N. T. Jafferis, E. F. Helbling, M. Karpelson, R. J. Wood, *Nature* **570**, 491–495 (2019).
9. Z. Ren et al., *Adv. Mater.* **34**, e2106757 (2022).
10. M. Dorigo, G. Theraulaz, V. Trianni, *Sci. Robot.* **5**, eabe4385 (2020).
11. A. Ghosh, B. Corves, *Introduction to Micromechanisms and Microactuators* (Springer, 2015), vol. 28 of *Mechanisms and Machine Science*.
12. W. S. N. Trimmer, *Sens. Actuators* **19**, 267–287 (1989).
13. R. J. Wood, S. Avadhanula, R. Sahai, E. Steltz, R. S. Fearing, *J. Mech. Des.* **130**, 052304 (2008).
14. Y. Chen et al., *Nature* **575**, 324–329 (2019).
15. D. J. Bell, T. J. Lu, N. A. Fleck, S. M. Sparing, *J. Micromech. Microeng.* **15**, S153–S164 (2005).
16. Z. Ma, D. Sameoto, *Micromachines* **13**, 1881 (2022).
17. N. T. Jafferis, K. Jayaram, P. A. York, R. J. Wood, *Sens. Actuators A Phys.* **332**, 113155 (2021).
18. M. Karpelson, G.-Y. Wei, R. J. Wood, "A review of actuation and power electronics options for flapping-wing robotic insects," 2008 *IEEE International Conference on Robotics and Automation*, Pasadena, CA, 19 to 23 May 2008, pp. 779–786; <https://doi.org/10.1109/ROBOT.2008.4543300>.
19. I. Morkvenaitė-Vilkonciene et al., *Micromachines* **13**, 1256 (2022).
20. X. Yue et al., *Adv. Mater.* **33**, e2101760 (2021).
21. A. C. Fernandez-Pello, *Proc. Combust. Inst.* **29**, 883–899 (2002).
22. H. Wang, Y. Yang, G. Lin, P. Jiao, Z. He, *Smart Mater. Struct.* **30**, 015035 (2021).
23. M. T. Tolley et al., "An untethered jumping soft robot," 2014 *IEEE/RSJ International Conference on Intelligent Robots and Systems*, Chicago, IL, 14 to 18 September 2014 (IEEE), pp. 561–566; <https://doi.org/10.1109/IROS.2014.6942615>.
24. R. F. Shepherd et al., *Angew. Chem. Int. Ed.* **52**, 2892–2896 (2013).
25. C. Stergiopoulos et al., "A Soft Combustion-Driven Pump for Soft Robots," *Proceedings of the ASME 2014 Conference on*

- Smart Materials, Adaptive Structures and Intelligent Systems*, vol. 2, Newport, RI, 8 to 10 September 2014 (American Society of Mechanical Engineers), p. V002T04A011; <https://doi.org/10.1115/SMASIS2014-7536>.
26. M. Loepte, C. M. Schumacher, W. J. Stark, *Ind. Eng. Chem. Res.* **53**, 12519–12526 (2014).
 27. R. H. Heisser et al., *Proc. Natl. Acad. Sci. U.S.A.* **118**, e2106553118 (2021).
 28. W. A. Churaman, L. J. Currano, C. J. Morris, J. E. Rajkowski, S. Bergbreiter, *J. Microelectromech. Syst.* **21**, 198–205 (2012).
 29. Y. Chen et al., *Sci. Robot.* **2**, eaao5619 (2017).
 30. M. Wehner et al., *Nature* **536**, 451–455 (2016).
 31. S. R. Turns, *Introduction to combustion* (McGraw-Hill Companies, 1996), vol. 287.
 32. W. Wang, Z. Zuo, J. Liu, *Energy Convers. Manage.* **112**, 101–114 (2016).
 33. caa243, caa243/Combustion-driven-microactuators: Main release, version 1.0, Zenodo (2023); <https://doi.org/10.5281/zenodo.7888443>.

ACKNOWLEDGMENTS

We thank M. Ulinski for his assistance in assembling experimental apparatuses and D. Woodie for coordinating safety efforts. **Funding:** Air Force Office of Scientific Research contract FA9550-20-1-0254 (R.F.S.); National Science Foundation contract EFMA-1830924 (R.F.S.); Office of Naval Research contract N00014-22-1-2595 (R.F.S.). **Author contributions:** Conceptualization: C.A.A. and R.F.S.; Methodology: C.A.A., R.H.H., O.P., and A.G.; Investigation: C.A.A., R.H.H., O.P., J.T., and J.L.; Visualization: C.A.A., R.H.H., O.P., J.T., and J.L.; Funding acquisition: A.D.G. and R.F.S.; Project administration: E.F.H., S.S., A.D.G., and R.F.S.; Supervision: E.F.H., S.S., A.D.G., and R.F.S.; Writing – original draft: C.A.A. and R.F.S.; Writing – review and editing: C.A.A., R.H., O.P., E.F.H., S.S., A.D.G., and R.F.S. **Competing interests:** The authors declare that they have no competing interests. **Data and materials availability:** All data are available in the main text or the supplementary materials. Code used in modeling our actuators, for controlling our experimental setup, and for controlling our high voltage electronics can be found online (33). **Licensing information:** Copyright © 2023 the authors, some rights reserved; exclusive licensee American Association for the Advancement of Science. No claim to original US government works. <https://www.science.org/about/science-licenses-journal-article-reuse>

SUPPLEMENTARY MATERIALS

science.org/doi/10.1126/science.adg5067
Materials and Methods
Supplementary Text
Figs. S1 to S17
Tables S1 to S6
References (34–103)
Movies S1 to S8

Submitted 1 January 2023; accepted 4 August 2023
10.1126/science.adg5067